Mathematical Biosciences and Engineering

MBE, 20(7): 11545–11567.
DOI: 10.3934/mbe.2023512
Received: 28 March 2023
Revised: 14 April 2023
Accepted: 16 April 2023
Published: 05 May 2023

http://www.aimspress.com/journal/MBE

Research article

Investigation on aortic hemodynamics based on physics-informed neural network

Meiyuan Du[1], Chi Zhang[1,2,*], Sheng Xie[3], Fang Pu[1,2], Da Zhang[4] and Deyu Li[1,2]

[1] Key Laboratory of Biomechanics and Mechanobiology, Beijing Advanced Innovation Center for Biomedical Engineering, School of Biological Science and Medical Engineering, Beihang University, No. 37 Xueyuan Road, Haidian District, Beijing 100083, China
[2] State Key Laboratory of Virtual Reality Technology and Systems, Beihang University, No. 37 Xueyuan Road, Haidian District, Beijing 100083, China
[3] Department of Radiology, China-Japan Friendship Hospital, Beijing, No. 2 Yinhua East Road, Chaoyang District, Beijing 100029, China
[4] Department of Physics, Sichuan Cancer Hospital, No. 55 South Renmin Road, Chengdu 610042, China

* **Correspondence:** Email: chizhang@buaa.edu.cn; Tel: +13401180593; Fax: +861082317114.

Abstract: Pressure in arteries is difficult to measure non-invasively. Although computational fluid dynamics (CFD) provides high-precision numerical solutions according to the basic physical equations of fluid mechanics, it relies on precise boundary conditions and complex preprocessing, which limits its real-time application. Machine learning algorithms have wide applications in hemodynamic research due to their powerful learning ability and fast calculation speed. Therefore, we proposed a novel method for pressure estimation based on physics-informed neural network (PINN). An ideal aortic arch model was established according to the geometric parameters from human aorta, and we performed CFD simulation with two-way fluid-solid coupling. The simulation results, including the space-time coordinates, the velocity and pressure field, were obtained as the dataset for the training and validation of PINN. Nondimensional Navier-Stokes equations and continuity equation were employed for the loss function of PINN, to calculate the velocity and relative pressure field. Post-processing was proposed to fit the absolute pressure of the aorta according to the linear relationship between relative pressure, elastic modulus and displacement of the vessel wall. Additionally, we explored the sensitivity of the PINN to the vascular elasticity, blood viscosity and blood velocity. The velocity and pressure field predicted by PINN yielded good consistency with the simulated values. In the interested region of the aorta, the relative errors of maximum and average absolute

pressure were 7.33% and 5.71%, respectively. The relative pressure field was found most sensitive to blood velocity, followed by blood viscosity and vascular elasticity. This study has proposed a method for intra-vascular pressure estimation, which has potential significance in the diagnosis of cardiovascular diseases.

Keywords: hemodynamics; fluid-structure interaction; physics-informed neural network; absolute pressure; aorta

1. Introduction

Abnormal cardiovascular flow is closely related to many cardiovascular diseases [1,2]. For example, the hemodynamic parameters in the aorta are of great significance for monitoring, diagnosis and surgical planning of aortic dissection, valve malformation and so on. It may reveal the mechanism, provide diagnostic indicators and evaluate treatment effects for cardiovascular diseases.

Direct measurement and computational fluid dynamics (CFD) have been possible methods for providing hemodynamic information in the cardiovascular system from different perspectives. For example, Swan and Ganz [3] proposed to send the catheters from peripheral arteries to the aorta, the end of which was connected to a monitoring manometry system to automatically display blood pressure values. Although the method is considered as the gold standard for intra-vascular pressure measurement, it is an invasive operation, limiting its application [4]. In recent years, non-invasive measurement technology has gradually been widely used in clinical practice, such as color Doppler flow imaging, 4D-flow magnetic resonance technology (4D-flow MRI) and so on. Through medical image processing [5–7], the non-invasive measurement of blood flow can provide more hemodynamic parameters, such as flow patterns, blood velocity, wall shear stress, etc., which can help doctors quantitatively diagnose vascular diseases.

However, non-invasive measurement has some limitations; for example, some key variables, such as pressure, are difficult to acquire. Therefore, CFD has received extensive attention in the field of hemodynamics. Blood flow in the circulatory system can be described by Navier-Stokes (NS) equations, which describe a highly nonlinear system in the form of partial differential equations (PDE). CFD makes PDE into algebraic equation groups through approximating the integral and differential terms to obtain numerical solutions at discrete time/space points. CFD combined with imaging technology can obtain the hemodynamic parameters of the flow in vessels. Recently, CFD has been used in the simulation of blood flow in different arteries of the human body [8–11]. However, there are some shortcomings, such as cumbersome preprocessing and high computational cost, which limit its application in clinical practice.

Recently, machine learning has shown more and more potential in the study of fluid mechanics. The current research on fluid mechanics based on neural networks is mainly divided into two categories: data-driven [12–15] and physics-informed [16–20]. Data-driven neural networks receive as input geometric features of vessels, and one expects to obtain the flow field solution by training the network with CFD simulation data. This method has higher requirements on the volume of dataset. At the same time, the training of the network requires a large amount of CFD calculation results as label data. The physics-informed neural network (PINN) is another approach to apply machine learning techniques to hemodynamic estimation. It integrates the fluid dynamics into the neural network, by

adding a set of PDE to the objective function of the optimization process. Similar networks have been developed to solve PDE problems not only in fluid mechanics, but also in electrical physics and molecular dynamics [21–23]. For example, Samaniego et al. explored deep neural networks as an option to approximate the solution of PDE in mechanical problems, by using the energy of a mechanical system as the loss function for a machine learning method. This method reduces the demand for data volume but increases the interpretability of neural networks.

The present work proposes a novel framework based on PINN [16,18] for estimating the absolute pressure in an ideal model of aorta. First, an ideal finite element model was established according to the parameters of the human aorta. The space coordinates, time and 3-dimensional velocity field required were obtained through two-way fluid-solid coupling algorithm. We preprocessed the above data and input it into the PINN to predict the relative pressure. Finally, the absolute pressure in aorta was obtained by fitting the relationship between wall displacement, vascular elastic modulus and relative pressure. On this basis, we also explored the sensitivity of the model to physical parameters such as blood velocity, vascular elasticity and blood viscosity. Compared with CFD, this method can directly use geometric information and flow field to predict absolute pressure. The advantage of the framework is agnostic to the geometry or the initial and boundary conditions, independent on the imposition of boundary conditions [18,24].

The main innovations of this work can be summarized in the following aspects:

1) As far as we know, this is a novel method to estimate pressure field with flow field and the displacement of vessel wall based on PINN. In addition, a post-processing step is added to calculate the absolute pressure in the vessel.

2) This paper explored the sensitivity of the network to physical parameters such as blood velocity, vascular elasticity and blood viscosity, revealing the stability of this network for pressure estimation.

2. Materials and methods

2.1. Two-way fluid-solid interaction

In this paper, we established an ideal aortic model based on real human data (Figure 1(a)) and performed fluid-solid-interaction (FSI) simulation to provide labeled data for a physically constrained machine learning network. The cross-sectional area of the blood vessel was about 2.27×10^{-4} m^2. The thickness of the vessel wall was assumed to be constant for the solid domain, taking the value of 1.2×10^{-3} m. The blood was assumed as incompressible laminar Newtonian fluid, while the vessel wall was simplified to linear elastic material. The FSI interface of the vessel satisfied the no-slip condition. Therefore, the movement of blood flow in the aorta satisfied the continuity equation and the 3-dimensional NS equation:

$$\nabla \cdot \mathbf{v} = 0 \tag{2.1}$$

$$\frac{\partial \mathbf{v}}{\partial t} + (\mathbf{v} \cdot \nabla)\mathbf{v} = -\frac{1}{\rho}\nabla p + \frac{\mu}{\rho}\nabla^2 \mathbf{v} \tag{2.2}$$

where $\mathbf{v}$ represents the blood flow velocity. In addition, t and p represent the time and the blood flow pressure, respectively, while ρ and μ denoted the density and viscosity of the blood, respectively.

The energy transfer equation at the FSI interface was as follows:

$$d_s = d_f \tag{2.3}$$

$$\boldsymbol{\sigma_s} \cdot \boldsymbol{n_s} = \boldsymbol{\sigma_f} \cdot \boldsymbol{n_f} \tag{2.4}$$

where d_s was the displacement at the solid boundary, and d_f was the displacement at the fluid boundary. $\boldsymbol{n_s}$ and $\boldsymbol{n_f}$ were the normal vectors at the solid and fluid boundary, respectively. $\boldsymbol{\sigma_s}$ and $\boldsymbol{\sigma_f}$ were the stress tensors at the vessel wall and fluid boundary, respectively.

The vessel wall satisfied the linear elasticity equation:

$$\boldsymbol{\sigma_s} \cdot \boldsymbol{n_s} = K \cdot d_s \tag{2.5}$$

where K was the equivalent stiffness of the vessel wall.

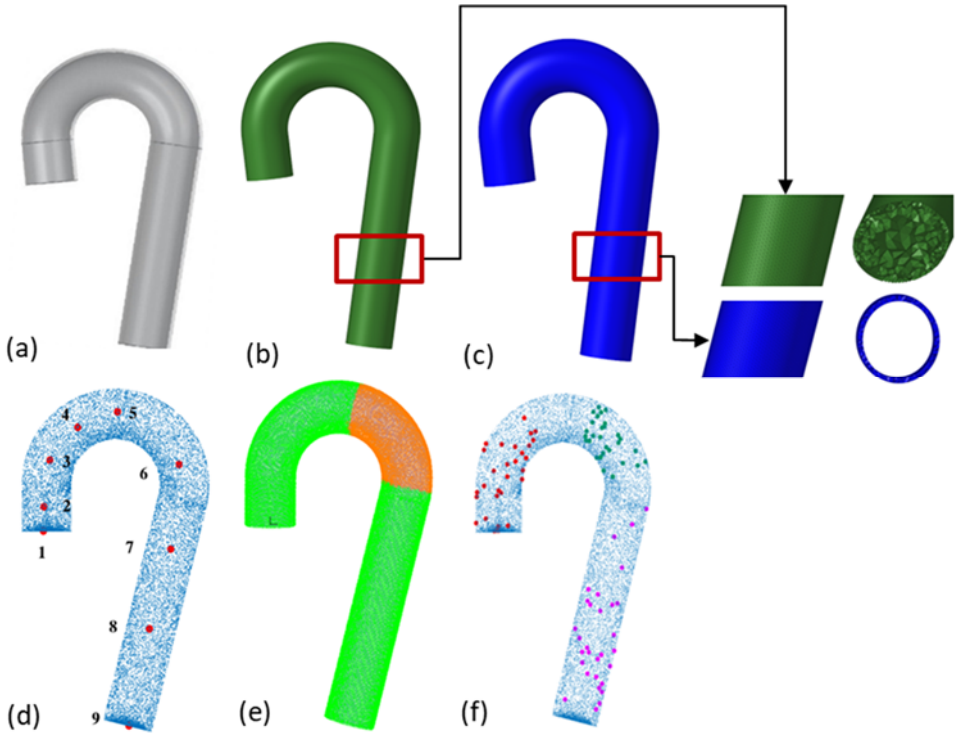

Figure 1. The ideal model of the aortic arch: (a) The ideal aortic arch model. (b) The fluid domain unit. The number of grids is 322,430. (c) The solid domain unit. The number of grids is 269,979. (d) The points selected for the validation of PINN. (e) The sample point set (brown points) used to fit the absolute pressure. (f) The test points for the validation of absolute pressure estimation. The red points correspond to 1-vessel inlet segment. The green points correspond to 2-vessel middle segment. The purple points correspond to 3-vessel outlet segment.

The finite element model of the aorta used tetrahedron elements to mesh the model. The fluid and solid domains of the model are shown in Figure 1(b),(c). The blood density was set to $1050\ \mathrm{kg/m^3}$. Blood viscosity coefficient was 0.0035 Pa·s. The elastic modulus of the blood vessel wall was 1.8 MPa. The

blood vessel density was 1060 kg/m^3, and Poisson's ratio was 0.45.

The blood in the vessel was a pulsatile flow. Therefore, the inlet of the vessel was set as a pulsatile speed function with a cardiac cycle of 0.8 s (Figure 2). The outlet was set as a free flow where the pressure was 0 Pa. For the solid domain, the inlet and outlet part of the vessel wall was fixed. The simulation was calculated for 4 cardiac cycles (0.8 s per cardiac cycle). The data from the last cycle was considered as the final simulation result. The calculation step was set to be 0.005 s.

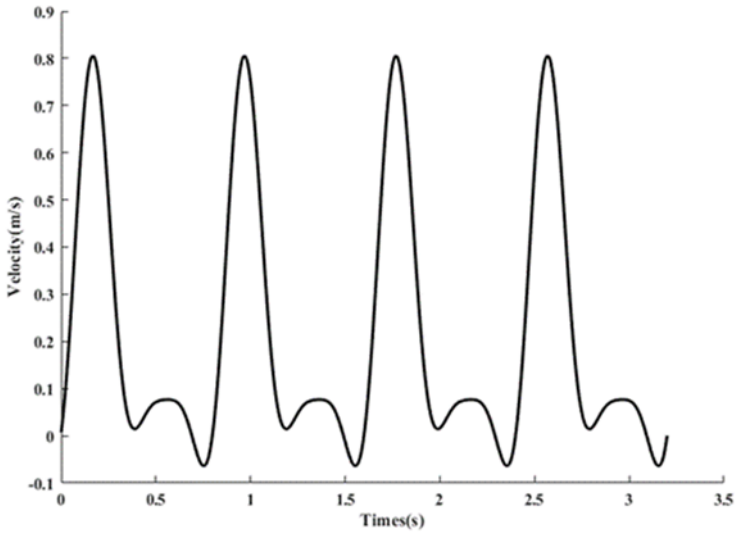

Figure 2. Velocity waveform of the inlet boundary of the aortic arch: Each cardiac cycle is 0.8 s.

2.2. Physics-informed neural networks

The physics-informed neural networks were to add the physical PDE equations describing the blood flow (3-dimensional NS equation and continuity equation) to the network framework as residual loss function in the network. The solutions of these PDE were obtained by training the network. The network defined the following mapping relationship:

$$[x, y, z, t] \longmapsto [u(x, y, z, t), v(x, y, z, t), w(x, y, z, t), p(x, y, z, t)] \tag{2.6}$$

The network loss function included measurement residual term, NS equation residual term and continuity equation residual term. The measurement residual term encouraged the output of the neural network u, v, and w to match the values of FSI calculation. The measurement loss function was expressed as follows:

$$L_{measurement} = \frac{1}{N}\sum_{i=1}^{N}[(u(x, y, z, t) - \hat{u}(x, y, z, t))^2 + (v(x, y, z, t) - \hat{v}(x, y, z, t))^2 + (w(x, y, z, t) - \hat{w}(x, y, z, t))^2] \tag{2.7}$$

where N was the number of sampling points in the blood vessel.

The NS equation loss function was as follows:

$$L_{NS} = \frac{1}{N}\sum_{n=1}^{N}(e_1 + e_2 + e_3)^2 \tag{2.8}$$

where

$$e_1 = \rho \cdot \left(\frac{\partial u}{\partial t} + u \cdot \frac{\partial u}{\partial x} + v \cdot \frac{\partial u}{\partial y} + w \cdot \frac{\partial u}{\partial z}\right) + \frac{\partial p}{\partial x} - \mu \cdot \left(\frac{\partial^2 u}{\partial x^2} + \frac{\partial^2 u}{\partial y^2} + \frac{\partial^2 u}{\partial z^2}\right),$$

$$e_2 = \rho \cdot \left(\frac{\partial v}{\partial t} + u \cdot \frac{\partial v}{\partial x} + v \cdot \frac{\partial v}{\partial y} + w \cdot \frac{\partial v}{\partial z}\right) + \frac{\partial p}{\partial y} - \mu \cdot \left(\frac{\partial^2 v}{\partial x^2} + \frac{\partial^2 v}{\partial y^2} + \frac{\partial^2 v}{\partial z^2}\right), \tag{2.9}$$

$$e_3 = \rho \cdot \left(\frac{\partial w}{\partial t} + u \cdot \frac{\partial w}{\partial x} + v \cdot \frac{\partial w}{\partial y} + w \cdot \frac{\partial w}{\partial z}\right) + \frac{\partial p}{\partial z} - \mu \cdot \left(\frac{\partial^2 w}{\partial x^2} + \frac{\partial^2 w}{\partial y^2} + \frac{\partial^2 w}{\partial z^2}\right).$$

The continuity loss function was as follows:

$$L_{continuous} = \frac{1}{N}\sum_{i=1}^{N}(u_x + v_y + w_z)^2 \tag{2.10}$$

Combining all loss function terms, the loss function of our PINN took the following form:

$$Loss = L_{measurement} + L_{NS} + L_{continuous} \tag{2.11}$$

In order to eliminate the influence of different physical quantity units and numerical values in the equation on the convergence speed of the network and speed up the training process, nondimensionalization and normalization was performed to the input of the network. Two characteristic variables commonly used in multi-scale physical models were introduced here: characteristic length L and characteristic velocity U. The diameter of the equilibrium cross-sectional area of the blood vessel was chosen as the characteristic length L; while the time-averaged velocity at the inlet was the characteristic velocity U. The variable form after becoming dimensionless was

$$\tilde{u} = \frac{u}{U}; \tilde{v} = \frac{v}{U}; \tilde{w} = \frac{w}{U}; \tilde{p} = \frac{p}{p_0}; \tilde{x} = \frac{x}{L}; \tilde{y} = \frac{y}{L}; \tilde{z} = \frac{z}{L}; \tilde{t} = \frac{t}{T}; \tag{2.12}$$

where $p_0 = \rho U^2$, $T = \frac{L}{U}$.

The network input variables x, y, z, t were standardized to the range (0,1) by the Z-Score method, namely,

$$x_* = \frac{\tilde{x}-\mu_{\tilde{x}}}{\sigma_{\tilde{x}}}; y_* = \frac{\tilde{y}-\mu_{\tilde{y}}}{\sigma_{\tilde{y}}}; z_* = \frac{\tilde{z}-\mu_{\tilde{z}}}{\sigma_{\tilde{z}}}; t_* = \frac{\tilde{t}-\mu_{\tilde{t}}}{\sigma_{\tilde{t}}}; \tag{2.13}$$

After the variables were nondimensionalized, the hemodynamic parameters estimated by the network were also nondimensional, which showed a need to multiply the nondimensionalization parameters before the final output, namely,

$$\hat{u} = \tilde{u}U; \hat{v} = \tilde{v}U; \hat{w} = \tilde{w}U; \hat{p} = \tilde{p}p_0. \tag{2.14}$$

At the same time, the loss function of the network would also change to the nondimensional form. The revised loss function of NS equation was

$$L_{NS} = \frac{1}{N}\sum_{n=1}^{N}(e_1' + e_1' + e_1')^2 \tag{2.15}$$

where

$$e_1' = \frac{1}{\sigma_{\tilde{t}}}\cdot\frac{\partial\tilde{u}}{\partial t_*} + \frac{1}{\sigma_{\tilde{x}}}\cdot\tilde{u}\cdot\frac{\partial\tilde{u}}{\partial x_*} + \frac{1}{\sigma_{\hat{y}}}\cdot\tilde{v}\cdot\frac{\partial\tilde{u}}{\partial y_*} + \frac{1}{\sigma_{\hat{z}}}\cdot\tilde{w}\cdot\frac{\partial\tilde{u}}{\partial z_*} = -\frac{1}{\sigma_{\tilde{x}}}\cdot\frac{\partial\tilde{p}}{\partial x_*} + Re^{-1}\left(\frac{1}{\partial^2\tilde{x}}\cdot\frac{\partial^2\tilde{u}}{\partial x_*^2} + \frac{1}{\partial^2\tilde{y}}\cdot\frac{\partial^2\tilde{u}}{\partial y_*^2} + \frac{1}{\partial^2\tilde{z}}\cdot\frac{\partial^2\tilde{u}}{\partial z_*^2}\right);$$

$$e_2' = \frac{1}{\sigma_{\tilde{t}}}\cdot\frac{\partial\tilde{u}}{\partial t_*} + \frac{1}{\sigma_{\tilde{x}}}\cdot\tilde{u}\cdot\frac{\partial\tilde{u}}{\partial x_*} + \frac{1}{\sigma_{\hat{y}}}\cdot\tilde{v}\cdot\frac{\partial\tilde{u}}{\partial y_*} + \frac{1}{\sigma_{\hat{z}}}\cdot\tilde{w}\cdot\frac{\partial\tilde{u}}{\partial z_*} = -\frac{1}{\sigma_{\tilde{x}}}\cdot\frac{\partial\tilde{p}}{\partial x_*} + Re^{-1}\left(\frac{1}{\partial^2\tilde{x}}\cdot\frac{\partial^2\tilde{u}}{\partial x_*^2} + \frac{1}{\partial^2\tilde{y}}\cdot\frac{\partial^2\tilde{u}}{\partial y_*^2} + \frac{1}{\partial^2\tilde{z}}\cdot\frac{\partial^2\tilde{u}}{\partial z_*^2}\right);\quad(2.16)$$

$$e_3' = \frac{1}{\sigma_{\tilde{t}}}\cdot\frac{\partial\tilde{u}}{\partial t_*} + \frac{1}{\sigma_{\tilde{x}}}\cdot\tilde{u}\cdot\frac{\partial\tilde{u}}{\partial x_*} + \frac{1}{\sigma_{\hat{y}}}\cdot\tilde{v}\cdot\frac{\partial\tilde{u}}{\partial y_*} + \frac{1}{\sigma_{\hat{z}}}\cdot\tilde{w}\cdot\frac{\partial\tilde{u}}{\partial z_*} = -\frac{1}{\sigma_{\tilde{x}}}\cdot\frac{\partial\tilde{p}}{\partial x_*} + Re^{-1}\left(\frac{1}{\partial^2\tilde{x}}\cdot\frac{\partial^2\tilde{u}}{\partial x_*^2} + \frac{1}{\partial^2\tilde{y}}\cdot\frac{\partial^2\tilde{u}}{\partial y_*^2} + \frac{1}{\partial^2\tilde{z}}\cdot\frac{\partial^2\tilde{u}}{\partial z_*^2}\right).$$

The modified loss function of continuity equation was

$$L_{continuous} = \frac{1}{N}\sum_{n=1}^{N}\left(\frac{1}{\sigma_{\tilde{x}}}\cdot\frac{\partial\tilde{u}}{\partial x_*} + \frac{1}{\sigma_{\tilde{y}}}\cdot\frac{\partial\tilde{v}}{\partial y_*} + \frac{1}{\sigma_{\tilde{z}}}\cdot\frac{\partial\tilde{w}}{\partial z_*}\right)^2 \quad (2.17)$$

Finally, different weights were assigned to the 3 terms of the loss function:

$$Loss = w_1 L_{measurement} + w_2 L_{NS} + w_3 L_{continuous} \quad (2.18)$$

where L_{NS} and $L_{continuous}$ were defined by Eqs (2.15) and (2.17); w_1:w_2:w_3 was fixed to 1:3:3 in this study.

The network was trained by the simulation data obtained from the finite element model of aorta. The simulated velocity and pressure could be regarded as physical quantities in the 4-dimensional space composed of space and time. There were 321 frames of velocity and pressure map in the time dimension, because the simulation data was obtained from a cardiac cycle (0.8 s), in which the interval between frames was 0.0025 s. The sampling points in the aortic model domain were 64,833, i.e., the total sample size was 321 × 64,833. These sample points were randomly divided in space according to the ratio of 3:1. The size of the training set was 321 × 48,625 and the size of the test set was 321 × 16,208. The network framework included an input layer, 10 hidden layers and an output layer. Each hidden layer had 50 neurons for each variable, and the batch size was 10,000. Mathematically, two adjacent layers are connected as

$$x_l = \sigma_l(\mathbf{W_l}\cdot x_{l-1} + b_l) \quad (2.19)$$

where $\mathbf{W}_l$ and b_l represented the weights vector and bias; the subscript l denoted the index of the layer; σ_l was the activation function expressed as a swish function:

$$\text{swish}(x) = x\cdot\text{sigmoid}(x) = x/(1-\text{e}^{-x}) \quad (2.20)$$

The learning rate $\eta = 10^{-3}$. The training lasted 30 h, using tensorflow on Intel(R) Xeon(R) GPU E5-2650 v4 @2.20 GHz training.

In this paper, the prediction results of the velocity field and pressure field from the network were compared with the ground value, which was obtained from the simulation results. In order to further evaluate the network performance, 9 points were selected from the inlet to the outlet of the model for quantitative evaluation. The 9 points were all located on the centerline of the model (Figure 1(d)). The relative L_2 error proposed by Raissi et al. was measured and the root mean square error (RMSE) as quantitative evaluation indicators [21]. The relative L_2 error was calculated as follows:

$$\varepsilon(f,g) = \left(\frac{1}{N}\sum_{i=1}^{N}[f(x_i)-g(x_i)]^2\right)/\left(\frac{1}{N}\sum_{i=1}^{N}[g(x_i)-\frac{1}{N}\sum_{i=1}^{N}g(x_i)]^2\right) \quad (2.21)$$

where f was the predicted value; g was the ground value. $\{x_i: i = 1,2,3 \ldots N\}$ was the spatial sample point. The RMSE was calculated as follows:

$$RMSE = \sqrt{\frac{1}{M}\sum_{i=1}^{M}[f(x_j) - g(x_j)]^2} \tag{2.22}$$

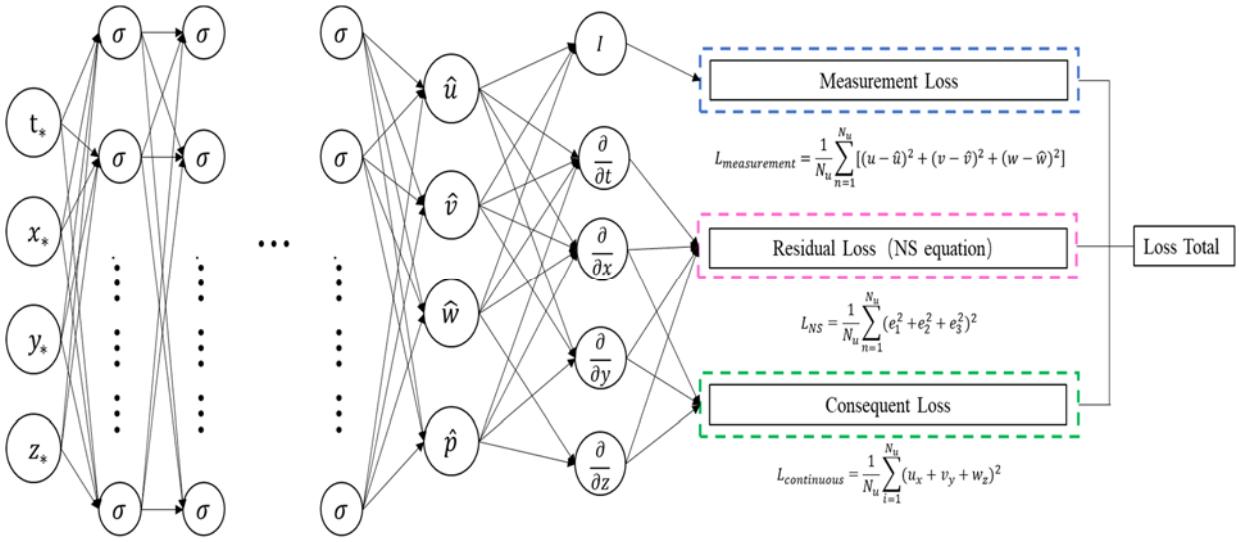

Figure 3. Physically constrained neural network framework.

2.3. Absolute pressure

The postprocessing of PINN was proposed to calculate absolute pressure from relative pressure obtained from PINN (Figure 4). In most cases, the absolute pressure was of more significance in clinical diagnosis. The pressure calculated by two-way FSI simulation was absolute pressure, which theoretically differed from the relative pressure predicted by the network with a constant term, namely:

$$P_{abs} = P_{rel} + b \tag{2.23}$$

where P_{abs} denoted the absolute pressure value, P_{rel} was the relative pressure value, and b was a constant term. The absolute pressure could be calculated with the displacement and the equivalent stiffness of the blood vessel wall:

$$P_{abs} = K \cdot n \tag{2.24}$$

where K denoted the equivalent stiffness of vessel, which equaled the elastic modulus multiplied by a length eigenvalue; and n was the normal displacement of the blood vessel wall. From Eqs (2.23) and (2.24), we could get:

$$P_{rel} = K \cdot n - b \tag{2.25}$$

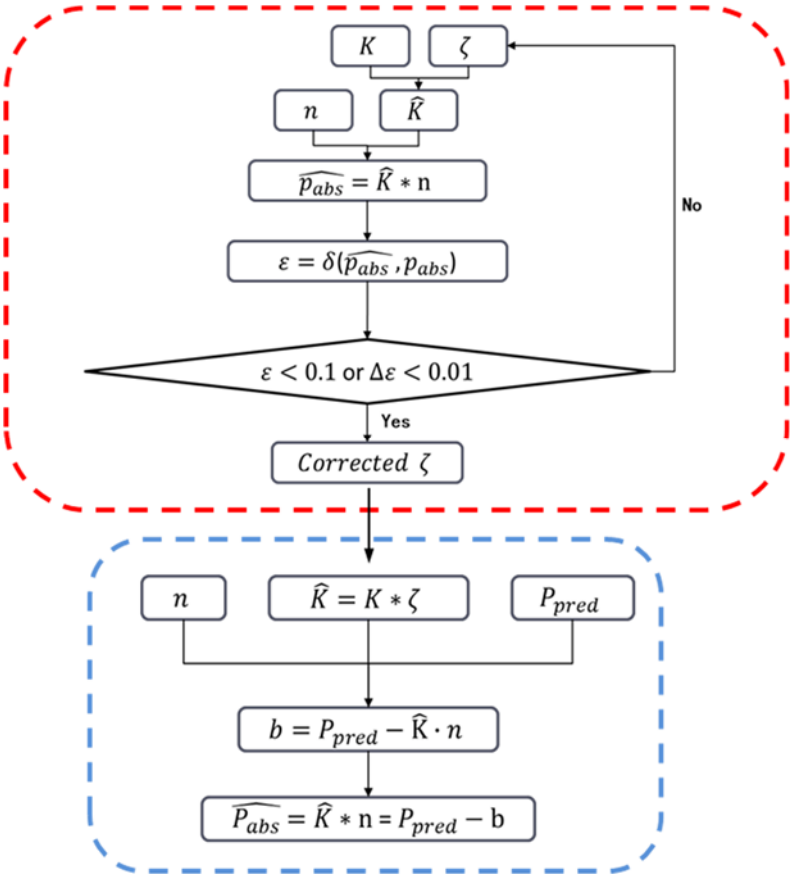

Figure 4. Fitting absolute pressure: the red box is the process of fitting ζ; the blue box is the process of fitting absolute pressure.

By fitting the b value of Eq (2.25), the P_{abs} could be calculated according to the P_{rel} predicted by the network.

However, the inlet and outlet of the blood vessel model was fixed during the FSI simulation, and the equivalent stiffness $\widehat{K}$ in Eq (2.26) was larger than the theoretic value K. It was assumed that there was a scaling factor between the real elastic modulus E and the equivalent stiffness $\widehat{K}$. To solve this problem, $\widehat{K}$ was estimated before the absolute pressure calculation. A scaling factor ζ was added, making the relationship between the real elastic modulus and equivalent stiffness as follows:

$$\widehat{K} = E * \zeta \tag{2.26}$$

In order to estimate ζ, the data points at the midsection of the vessel were selected to fit ζ from Eq (2.26) (Figure 1(e)). The correction coefficient was determined by reducing the gap between the theoretical absolute pressure and the simulated absolute pressure gradually. The corresponding steps were as follows:

The relative distance between the absolute pressure and the simulated absolute pressure was defined as $= \frac{|\widehat{P_{abs}} - P_{abs}|}{P_{abs}}$. Adjust ζ each time in the direction of reducing ε, until the relative distance $\varepsilon < 10\%$ or $\Delta\varepsilon < 1\%$. The update formula of ζ was as follows:

$$Corrected\ \zeta = \zeta * (1 \pm 0.01) \tag{2.27}$$

The vessel was divided into 3 parts according to the position, in which the midsection was used to fit the correction coefficient and absolute pressure, with the other 2 parts to verify the result. In this paper, we used Arabic numerals to mark 3 test sets: 1-vessel inlet segment, 2-vessel middle segment, 3-vessel outlet segment. Thirty points were randomly selected in each segment to evaluate the predicted absolute pressure (Figure 1(f)).

2.4. Sensitivity analysis

In the work, the sensitivity of PINN was tested with 3 parameters, including vascular elasticity, blood viscosity and blood velocity, which usually varied greatly between patients. The sensitivity index was defined as the ratio of the relative change of the average RMSE to the relative change of the physical parameter (Eq (2.28)). The higher the index, the more sensitive PINN was to this parameter. Each variable was changed to 5 levels to calculate the sensitivity index (Table 1). The range of the parameters referred to published literature, corresponding to the different pathological statuses, such as hyperlipidemia and atherosclerosis [25,26].

$$\tau = \frac{|\Delta RMSE|}{RMSE} / \frac{|\Delta x|}{x} \tag{2.28}$$

where τ was sensitivity index; x were physical parameters such as blood flow velocity, blood viscosity or elastic modulus.

Table 1. Physical parameter settings for sensitivity analysis.

Group	1	2	3	4	5
peak blood velocity (m/s)	0.4	0.6	0.8	1.0	1.2
blood viscosity (Pa·s)	0.0025	0.0030	0.0035	0.0040	0.0045
vascular elasticity (Mpa)	1.0	1.4	1.8	2.2	2.7

The method of migration learning was used to reduce the time cost of training. The model with the data of Group 3 was used as the pre-training model. The network of remaining groups was fine-tuned on the basis of the pre-trained model. The process could be defined as:

$$D(s) = \{\chi, P(\chi)\}, D(t) = \{\chi, P(\chi)\} \tag{2.29}$$

where $D(s)$ was the source domain; $D(t)$ was the target domain; χ was the feature space of domain data; $P(\chi)$ was the marginal probability distribution corresponding to the domain data feature space (Figure 5).

The data of group 3 was considered as the source domain $D(s)$, and the remaining group data was as the target domain $D(t)$. In this work, $D(s) \neq D(t)$, but the learning tasks of the source domain and the target domain were the same. So, the architecture and weight parameters of the pre-training model were kept as the learning starting point of the second task model. In order to avoid oscillation in the fine-tuning process, a smaller learning rate was used in fine-tuning training. The learning rate $\eta = 10^{-5}$, and the batchsize was adjusted to 5000.

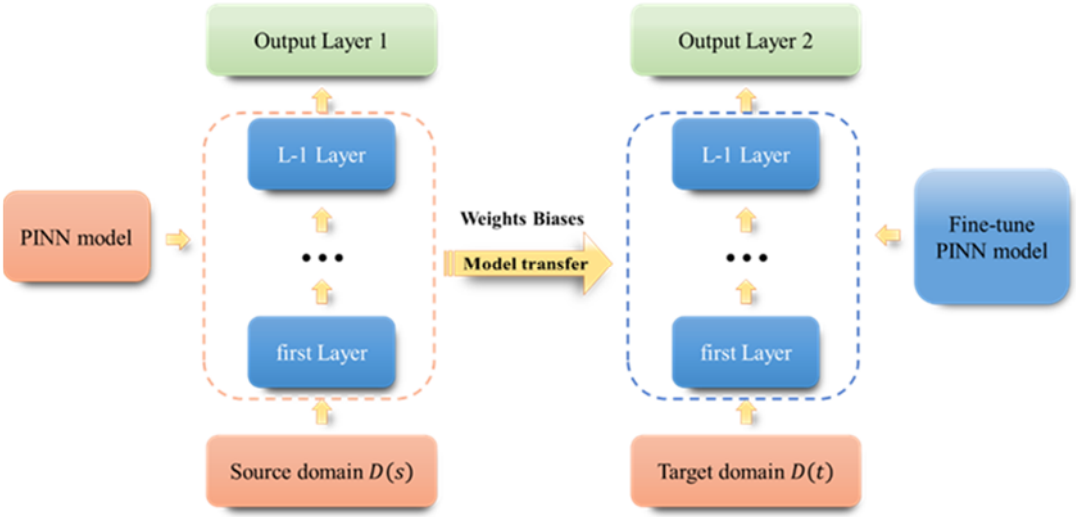

Figure 5. Flow chart of transfer learning.

Migration learning on the basis of the pre-trained model was performed for 1, 20 and 30 hours, respectively. The duration for migration learning was determined by comparing the loss-iteration curve of migration learning and the average RMSE of the prediction results of 9 test points.

3. Results

3.1. Two-way fluid-solid interaction

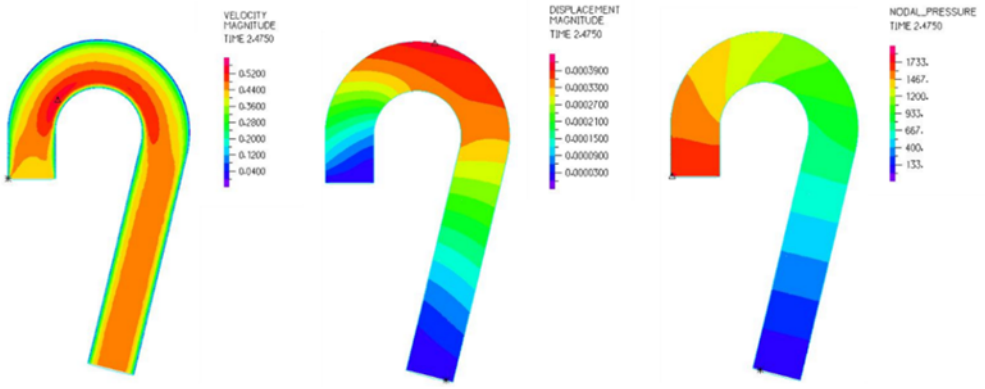

Figure 6. The simulation results of two-way fluid-solid interaction at the time of peak velocity (t = 2.475 s); (a) velocity cloud (Unit: m/s); (b) displacement cloud (Unit: m); (c) pressure cloud (Unit: Pa).

FSI simulation reached convergence after about 48 hours. Figure 6 shows the velocity contour, displacement contour and pressure contour at the peak moment of blood flow velocity in the fourth cardiac cycle (t = 2.475 s) of two-way fluid-solid interaction. It could be found that the flow velocity calculated by the PINN conformed to the Poiseuille flow. The blood flow velocity at the center was relatively high, and the blood flow velocity near the wall was close to 0, which was consistent with the no-slip setting of the wall in our simulation. Since the inlet and outlet were set with displacement

constraints, the displacement of the vessel was 0 at the inlet and outlet. The pressure basically had a gradient distribution from the inlet to the outlet. The pressure near the outlet was 0, which met the outlet boundary conditions set during the simulation. The distribution of velocity and pressure and the gradient showed good consistency with the pattern reported already [27–29].

3.2. Flow field estimated by PINN

Figure 7 shows the result profile of test set at the peak velocity moment (t = 2.475 s). It showed that, comparing with the ground value, the network prediction results and the simulation data showed good consistency in light of the velocity amplitude and the pressure gradient distribution. It should be noted that the bias between the pressure fields obtained by PINN and simulation was relatively large, because NS equations included in the loss function of PINN only revealed the relationship between the velocity of flow and the relative pressure, instead of the absolute pressure.

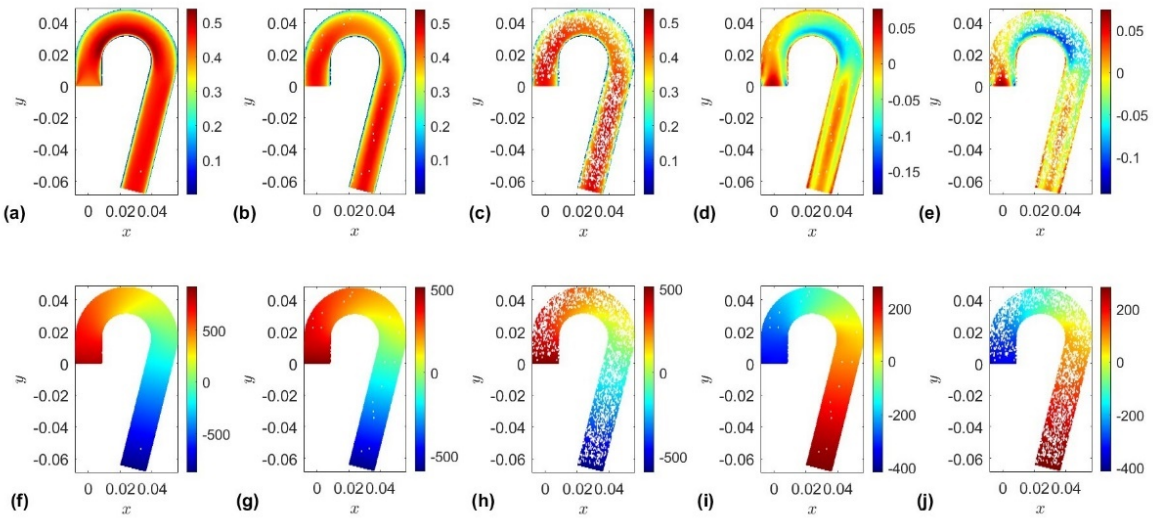

Figure 7. Comparison between velocity and pressure results obtained by PINN and simulation at t = 2.475 s. The first line denotes the velocity field (unit: m/s); the second denotes the pressure field (unit: Pa). (a)–(e) represent the simulated velocity field, the velocity estimated by PINN with the training set, the velocity estimated by PINN with the test set, the bias of velocity from the training set, the bias of velocity from the test set, respectively. (f)–(j) represent the simulate pressure field, the pressure estimated by PINN with the training set, the pressure estimated by PINN with the test set, the bias of pressure from the training set, the bias of pressure from the test set, respectively.

Figure 7 showed the performance of flow field estimation in the whole test set. In order to evaluate the results quantitatively, 9 points were selected from the test set (Figure 1(d)). A comparison waveform between the predicted value and the ground value in a cardiac cycle is drawn in Figure 8. Theoretically, there was a constant difference between the predicted pressure and the simulated pressure. In order to better display the results, we normalized the simulated and predicted values of the pressure to limit their size in the same range.

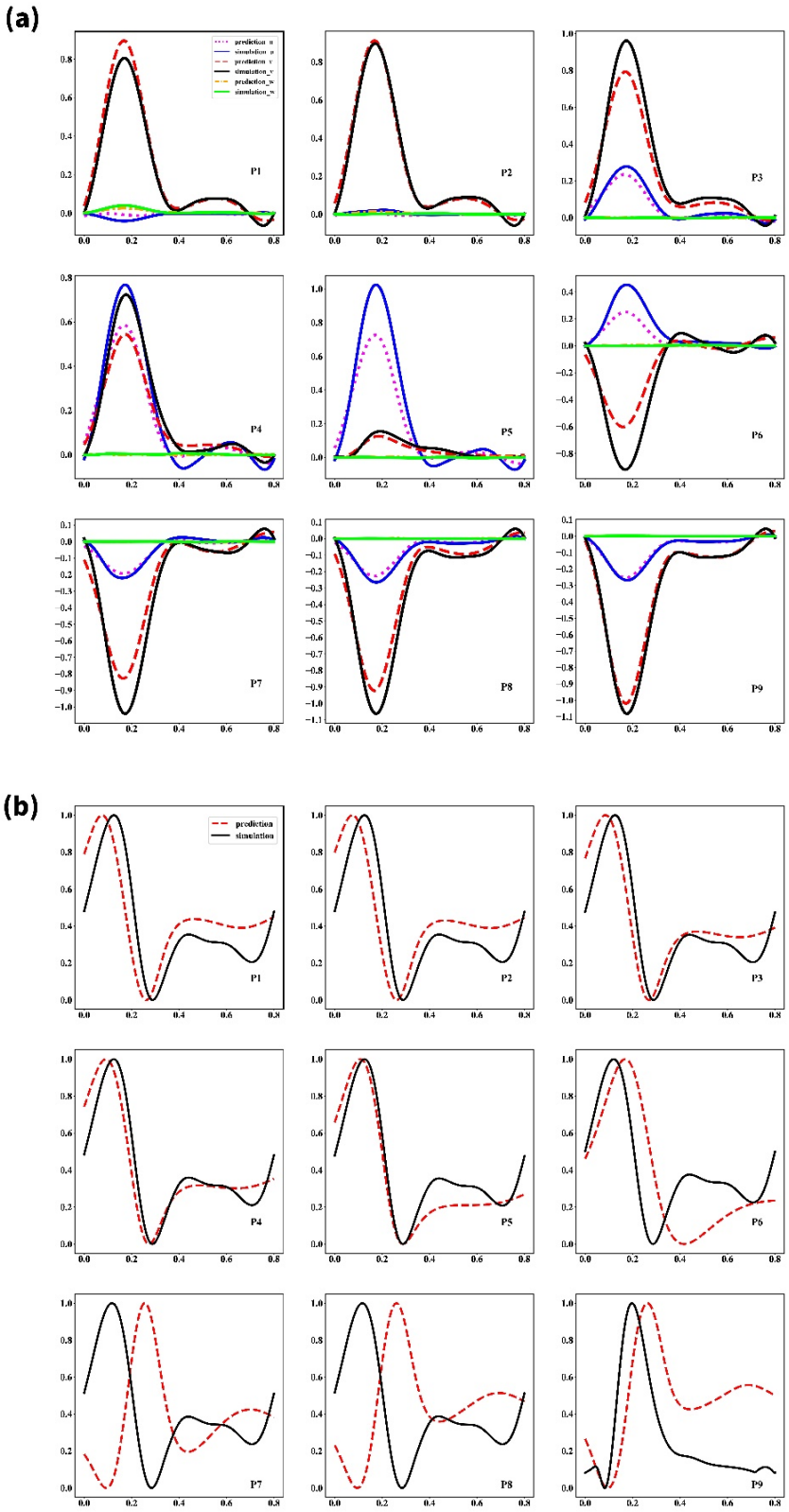

Figure 8. Comparison between velocity and pressure obtained by PINN and FSI simulation at 9 test points. (a) The velocity in x, y, z directions, namely u, v, w (m/s). u and w are perpendicular to the inlet velocity; v is parallel to the inlet velocity. (b) The normalized pressure. The abscissa is time: t (s).

It could be seen from Figure 8 that the predicted velocities in x, y, z directions were basically consistent with the ground values, where only small errors could be observed at very few moments. The result also showed that the normalized pressure value of points 1–6 is consistent with the ground value. There was a certain error at $t \in$ (2.8 s, 3.2 s), but the relative value of the error was acceptable. The waveform of normalized predicted pressure at points 7–9 was similar to the ground value, but there was a large phase difference, which might be because the pressure of the points near the outlet was greatly affected by the outlet boundary conditions. At the same time, the RMSE of the velocity prediction in each direction at 9 points is shown in Table 2.

Table 2. RMSE of Estimated velocity in x, y, z directions of 9 test points.

Points	u	v	w	Velocity Amplitude
1	0.0138	0.0415	0.0056	0.0409
2	0.0088	0.023	0.0055	0.0229
3	0.0235	0.0772	0.0014	0.0803
4	0.0825	0.0776	0.0031	0.1112
5	0.1282	0.0167	0.0025	0.1280
6	0.0882	0.1381	0.0023	0.1618
7	0.0169	0.0982	0.0006	0.0983
8	0.0185	0.0724	0.0006	0.0746
9	0.0093	0.0352	0.0005	0.0362
Mean	0.0433	0.0644	0.0025	0.0838

The average predicted RMSE of the 9 test points in x, y, z directions were 0.0433, 0.0644 and 0.0025 m/s, respectively. Considering that the velocity amplitudes was about 0.8 m/s, it could be shown that the prediction result of the velocity was relatively accurate (mean relative error: 10.5%). In order to further evaluate the prediction error relative to the magnitude of the velocity, the relative L_2 error calculated by Eq (2.19) within one cardiac cycle is shown in Figure 9.

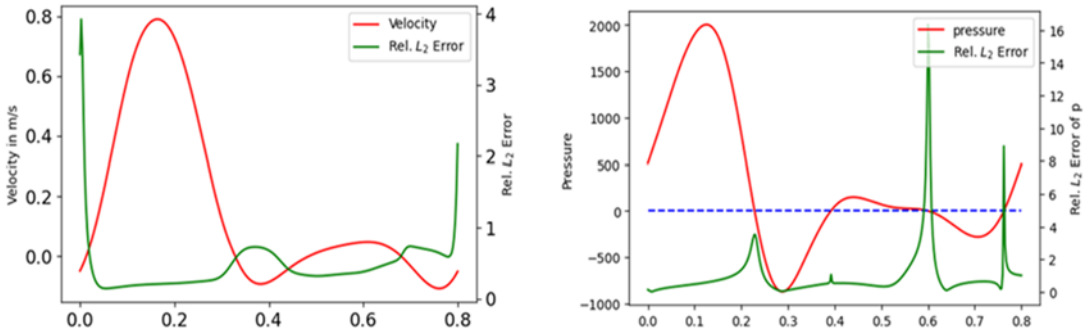

Figure 9. Average relative L_2 error of predicted velocity amplitude and pressure for all test points.

From Figure 9, it could be seen that the relative L_2 error between the velocity amplitude and the pressure was small in most of a cycle. The position with a large relative error corresponded to the velocity or pressure value close to 0, making it reasonable because L_2 measures the relative error of the velocity and pressure estimation.

3.3. Absolute pressure

The displacement and absolute pressure of the points in Figure 1(e) was used to fit the correction coefficients for each elastic parameter expressed by Eq (2.25). The results were shown in Table 3. The mean value of the correction coefficients of the 5 groups was considered as elastic modulus correction coefficient of vessel.

Table 3. The correction coefficients of different elastic modulus models.

	1.0 MPa	1.4 MPa	1.8 MPa	2.2 MPa	2.7 MPa	Mean
ζ	1.52	1.51	1.50	1.49	1.49	1.50

According to Eq (2.25), the actual elastic modulus coefficients of a vessel in each group could be obtained from ζ and the elastic modulus value initially set in the simulation E. Table 4 presented the actual elastic modulus coefficients $\widehat{K}$ and the estimated constant difference between the absolute pressure and the relative pressure $\hat{b}$ expressed by Eq (2.23), according to which, the absolute pressure was fitted and then verified with the simulation data at the 3-part point sets in Figure 1(f). The evaluation results for Bland-Altman consistency between the absolute pressure and the predicted pressure were shown in Figure 10, including the maximum and average value over one cardiac cycle. It could be found that no matter whether it was the maximum pressure or the average pressure, the error of pressure estimation was related to the pressure level. In the segment near the outlet, the pressure tended to be overestimated, while in the segment near the entrance, the pressure tended to be underestimated. It also showed that only the points located at the middle section of the vessel had a mean difference near 0 between the ground value and the fitted value. The difference between the mean values of the two groups of pressures at the inlet and outlet was relatively large, because the hemodynamic parameters at the inlet and outlet were greatly affected by the boundary conditions of the simulation.

Average relative errors of the absolute pressure predictions at 3 vessel segments are shown in Table 5. The average relative error of the outlet was extremely large, which was the same as the result of the Bland-Altman consistency analysis, also caused by the influence of boundary conditions in simulation.

Table 4. Equivalent stiffnesses and estimated constants of different models.

Elastic Modulus	1.0 MPa	1.4 MPa	1.8 MPa	2.2 MPa	2.7 MPa
$\widehat{K}(MPa/m)$	1.50	2.10	2.52	3.30	4.05
$\hat{b}(Pa)$	-974.23	-970.51	-892.04	-972.66	-973.06

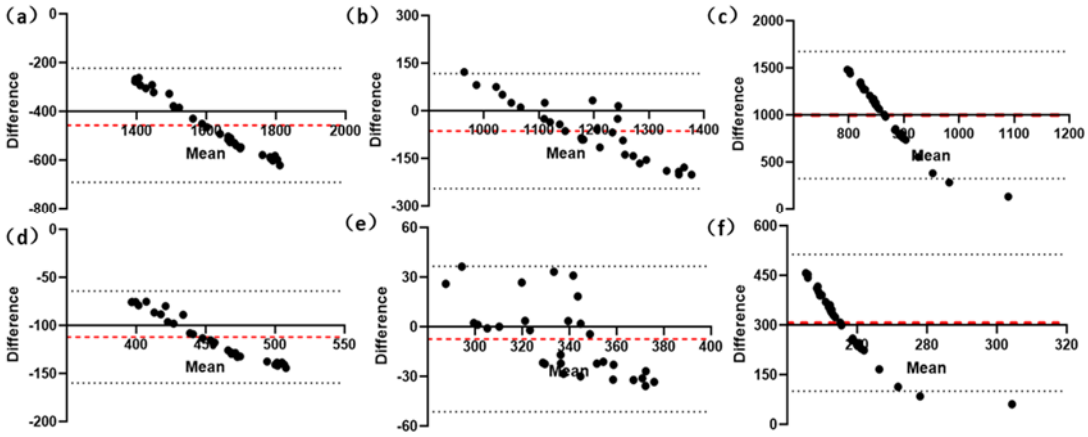

Figure 10. Consistency evaluation (maximum absolute pressure & average absolute pressure) between predicted value and ground value at different vessel segment; (a–c) represent the consistency evaluation results of maximum absolute pressure at 1-vessel inlet segment, 2-vessel middle segment and 3-vessel outlet segment, respectively; (d–f) represent the consistency evaluation results of the mean absolute pressure.

Table 5. Average relative error of absolute pressure prediction for different segment.

average relative error	1	2	3
P_{max}	24.44%	7.33%	528.23%
P_{mean}	21.80%	5.71%	569.83%

3.4. Transfer learning

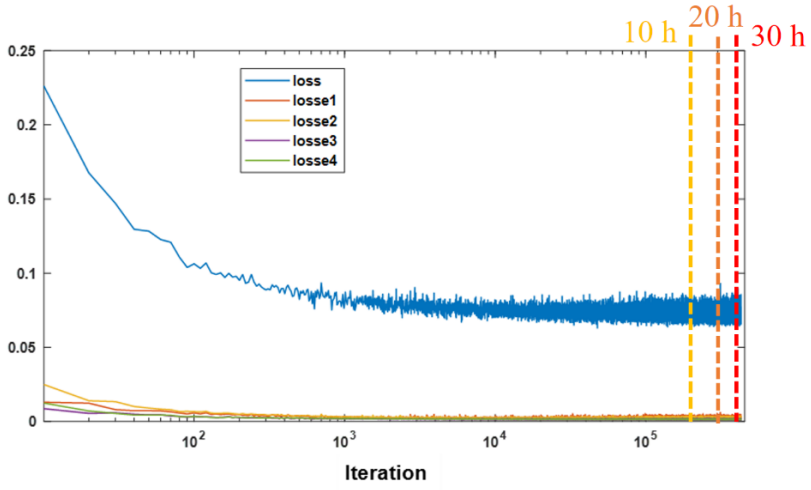

Figure 11. The residual curve of transfer learning. loss is the total residual; *losse1* is the measurement residual of u; *losse2* is the measurement residual of v; *losse3* is the measurement residual of w; *losse4* is the residual of the physical equation. The yellow dotted line represents 10 hours, while the orange and red dotted lines represent 20 and 30 hours, respectively.

The transfer training residual curve for 10 hours of migration learning is shown in Figure 11, and the average RMSE of the prediction results of 9 points were compared between 10, 20, and 30 hours of migration learning, respectively (Table 6). The loss-iteration curve showed that the model had converged after training for 10 hours. The MSE of 10 hours of transfer learning was very close to 20 and 30 hours. Considering the time cost of calculation, we chose 10 hours of transfer learning in this work.

Table 6. Prediction results from different durations of transfer learning.

	u	v	w	Velocity Amplitude	$\bar{P}_{normal}$
RMSE (10 h)	0.0614	0.0754	0.0032	0.0960	0.0796
RMSE (20 h)	0.0612	0.0754	0.0032	0.0958	0.0800
RMSE (30 h)	0.0612	0.0754	0.0032	0.0958	0.0797
RMSE (No transfer learning)	0.0604	0.0748	0.0031	0.0948	0.0775

Note: $\bar{P}_{normal}$ is the average normalized relative pressure. *No transfer learning* means no training on the basis of source domain, but training directly from the initial state for 30 hours.

3.5. Sensitivity analysis

In this work, we analyzed the sensitivity of velocity estimation and pressure estimation to the elastic modulus, blood viscosity and blood velocity. The sensitivity curves for each variable in Figure 12 display that the sensitivity of pressure estimation to vascular elasticity, blood viscosity and blood velocity increased in turn, but most of the sensitivity coefficients were within 10%, and only when the change of blood velocity exceeded 20% would it causes a large fluctuation in the prediction of networks.

In addition, the velocity estimation was most sensitive to blood velocity parameters, subsequently sensitive to blood viscosity and vascular elasticity equally. The velocity prediction performance of the network hardly changed with changes in blood viscosity and vascular elasticity. All the above showed that the model had strong stability in speed and pressure estimation within a certain range.

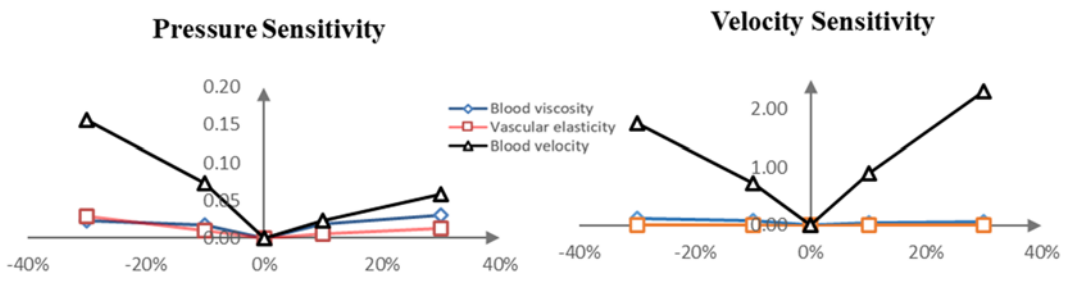

Figure 12. Sensitivity analysis curves of velocity and pressure estimation to vascular elasticity, blood viscosity and blood velocity.

4. Discussion

In this work, we established a novel method for the intra-vascular absolute pressure estimation based on PINN, by inputting a velocity field of fluid and a deformation field of vessel wall. The velocity of blood flow in the vessels can be obtained by some medical imaging technology, as well as the vascular deformation, showing the application potentials of our method. For example, the velocity field of blood flow can be non-invasively acquired by 4D-flow MRI, while the vascular deformation can be measured by time-of-flight MRI. However, we have to admit that the estimation accuracy of our method relies on the resolution of imaging, namely, the data points containing the information of velocity and deformation field. Nowadays, the resolution of images is not so high as to provide enough data points for the PINN training. Therefore, we have used simulation data for the PINN training to validate the availability of this method in the present work. We have built an ideal aortic arch model and conducted two-way fluid-structure interaction simulation, from which, the velocity field of flow and the displacement of vessel are obtained for the estimation of absolute pressure in the aorta. Meanwhile, we also explored the sensitivity of the network to the vascular elasticity, blood viscosity and blood velocity. The results showed that the network was robust to vascular elasticity and blood viscosity. This paper provided a new method for the estimation of intravascular pressure, which could provide a reference for the noninvasive diagnosis of diseases that rely on intravascular pressure.

The PINN provides better interpretability for neural networks and avoids the cumbersome process of CFD. Kissas et al. [16] used blood flow velocity and vessel wall displacement to train a PINN to calculate pressure waveform propagation of bifurcated vessel. However, this method simplifies the bifurcated vessel into a one-dimensional space. Therefore, only one-dimensional hemodynamic information along the vessel could be obtained. Raissi et al. [18] constructed a similar network to calculate the 3D flow field by using the time-space distribution of the dye concentration at a given time-space sampling point. The method could be used in the calculation of the flow field in aneurysm models. However, it is difficult to obtain the tracer dye concentration in human vessels in vivo, which limits the further application of this method.

To overcome the shortcomings mentioned above, we have proposed an approach to obtain the absolute pressure in aorta from the velocity field and the displacement of vessel wall, which could be imaged by medical imaging technology, such as Doppler ultrasound and 4D-flow MRI. Our method added post-processing to PINN, mining the hemodynamic information from the interaction between the vessel wall and blood flow. In contrary to CFD, the absolute pressure field obtained by our method is independent of the boundary conditions. According to the linear relationship between the relative pressure and absolute pressure, the absolute pressure is fitted with the relative pressure field from PINN, as well as the wall displacement, which could be obtained by non-invasive imaging technologies in clinical practice. Although the data used for the training of PINN in this paper are all from CFD, it is expected to use 4D-flow MRI or other imaging methods to non-invasively obtain the velocity field as label data in the future.

The comparison between the velocity and pressure field obtained by our method and FSI simulation shows a high consistency, indicating that our PINN-based method has a similar performance with CFD in revealing the fluid field in large vessels, while the time consumption of our method is less (about 10 h vs. 48 h). The mean relative error of the velocity estimation is about 10.5%. Furthermore, the relative L_2 error is calculated to describe the error between the predicted hemodynamic factors and the ground value. This relative error L_2 stays at a very low level at the most over the cardiac cycle, unless the

velocity or pressure is near 0, showing a similar result comparing with Raissi's work [18]. The error of pressure estimation was also low (7.33% and 5.71% for the maximum and average absolute pressure estimation, respectively), suggesting the potential availability of this method in the diagnosis of cardiovascular diseases. The outperformance of the PINN may be attributed to the following 3 aspects: First, different from other NN, our PINN added the equations describing the fluid mechanics in the loss function, making the network learn the information from not only the training data but also the physical theory. Second, FSI simulation provides sufficient and noise-free training data for PINN (about 2.1×10^7 data points, 10^4 times more than the number of neurons in PINN), making the network well trained. Third, the sufficient depth and size of network has been proved helpful to reduce the error in test dataset [18].

The error of absolute pressure prediction by our method displays a heterogeneous distribution. This may be attributed to the fact that the boundary conditions in FSI have great influence on the accuracy of pressure estimation. At the sampling points near the outlet (points 7–9), there is a large phase difference between the predicted pressure and the ground value, which may be due to the fact that the pressure is greatly affected by the boundary conditions of the outlet. The accuracy of absolute pressure prediction is also correlated with the location of points. The value is more likely to be underestimated at the site with high pressure. The relative error is less than 10% in the middle segment and 20–25% at inlet. The value is more likely to be overestimated at the segment with low pressure, which is likely caused by the boundary of the outlet being a free boundary ($P = 0$ Pa).

In addition, we have explored the sensitivity of the method to the vascular elasticity, blood viscosity and blood flow velocity. It has been found that the sensitivity of the pressure estimation obtained by PINN to the vascular elasticity, blood viscosity and blood flow velocity increases in turn. The velocity estimation is most sensitive to the blood flow velocity. The results show that the method has strong robustness when vascular elasticity and blood viscosity are within a reasonable range. On the other hand, the results also suggest that the accuracy of this method mainly relies on the accuracy of the blood flow velocity measurement.

This work still has some limitations in the following aspects:

1) The method is applied in the ideal aorta model currently, trained with the simulation data. The performance of the absolute pressure estimation by the PINN-based method is highly dependent on the amount and quality of training data, like other neural networks. The FSI simulation in our study provides sufficient and noise-free data for the training of PINN, ensuring the relative error of pressure estimation by our method was lower than 10%. However, there are still some difficulties to apply this method in clinical practice, because the low resolution and noise of blood flow imaging limit the availability of the data points containing the velocity field in the training of PINN. To realize the application of this method in practice, the dimensionality reduction of the network is needed to reduce the requirement of this method on the image resolution.

2) The results of FSI simulation also constrained the accuracy of pressure estimation, because the simulation is based on some assumptions; for example, the blood flow is simplified to laminar flow, while the outlet is set as a free outflow [21,30]. Compared with Savabi's research on FSI simulation of aortic arch, our results show good consistency in the velocity distribution and pressure gradient [31]. On the other hand, the displacement of vessel wall in our results was uniformly less than that shown in Savabi's work, because the elastic modulus of the vessel wall set in our research was larger. Therefore, the FSI simulation results should be reliable in our research. Nevertheless, the FSI simulation may become more complex when processing the vessels with large tortuosity or bifurcations, because the

complicated morphology of the vessel induces more turbulence in the flow, which requires introducing turbulence modeling to the fluid mechanics simulation. The PINN-based method for the pressure estimation in these vessels with complicated morphology may also need to add the equations of a turbulence model, which should be further studied.

3) We have tried to choose the neural networks' architectures in a consistent fashion throughout the manuscript. However, there might exist some approaches to improve the architecture by hyper-parameter tuning techniques and more broadly meta-learning. For example, Guo and Zhuang have proposed the hyperparameter optimization method to improve the performance of PINN [32,33]. On the other hand, the weights for the different terms in the loss function of PINN are fixed in the present study. However, the PINN is a multitask learning network. The weight coefficients of each task in the loss function need to be adjusted to obtain the optimum results for pressure estimation. Kendall et al. [34] have proposed an approach to multitask deep learning network which weighs multiple loss functions by considering the homoscedastic uncertainty of each task. This allows them to simultaneously learn various quantities with different units or scales in both classification and regression settings. It may be an important direction for PINN in future study [35,36].

5. Conclusions

In summary, this work makes it possible to use velocity field information, wall displacement and elastic modulus to obtain the absolute pressure. Through the verification of simulation data, this method is feasible. The accuracy of pressure estimation mainly depends on the measurement accuracy of the velocity field, while it is relatively robust to blood viscosity and vascular elasticity. In the future, this method is expected to play an important role in the diagnosis of vascular diseases such as arterial hypertension and atherosclerosis.

Acknowledgments

The study was supported by the key research and development project of Sichuan Province (2022YFS0029) and State Key Laboratory of Virtual Reality Technology and Systems.

Conflict of interest

The authors declare there is no conflict of interest.

References

1. M. Kadem, L. Garber, M. Abdelkhalek, B. K. Al-Khazraji, Z. Keshavarz-Motamed, Hemodynamic modeling, medical imaging, and machine learning and their applications to cardiovascular interventions, *IEEE Rev. Biomed. Eng.*, **16** (2023), 403–423. https://doi.org/10.1109/RBME.2022.3142058
2. M. F. O'Rourke, A. Adji, W. W. Nichols, C. Vlachopoulos, E. R. Edelman, Application of arterial hemodynamics to clinical practice: a testament to medical science in London, *Artery Res.*, **18** (2017), 81–86. https://doi.org/10.1016/j.artres.2017.03.003

3. K. Chatterjee, The swan-ganz catheters: past, present, and future: a viewpoint, *Circulation*, **119** (2009), E548. https://doi.org/10.1161/CIRCULATIONAHA.109.192583
4. R. Kett-White, P. J. Hutchinson, P. G. Al-Rawi, A. K. Gupta, J. D. Pickard, P. J. Kirkpatrick, Adverse cerebral events detected after subarachnoid hemorrhage using brain oxygen and microdialysis probes, *Neurosurgery*, **50** (2002), 1212–1221. https://doi.org/10.1097/00006123-200206000-00008
5. P. van Ooij, W. V. Potters, J. Collins, M. Carr, J. Carr, S. C. Malasrie, et al., Characterization of abnormal wall shear stress using 4D flow MRI in human bicuspid aortopathy, *Ann. Biomed. Eng.*, **43** (2015), 1385–1397. https://doi.org/10.1007/s10439-014-1092-7
6. Y. Qin, J. H. Wu, Q. M. Hu, D. N. Ghista, K. K. L. Wong, Computational evaluation of smoothed particle hydrodynamics for implementing blood flow modelling through CT reconstructed arteries, *J. X-ray Sci. Technol.*, **25** (2017), 213–232. https://doi.org/10.3233/XST-17255
7. V. M. Pereira, B. Delattre, O. Brina, P. Bouillot, M. I. Vargas, 4D flow MRI in neuroradiology: techniques and applications, *Top. Magn. Reson. Imaging*, **25** (2016), 81–87. https://doi.org/10.1097/RMR.0000000000000082
8. K. Y. Lin, T. C. Shih, S. H. Chou, Z. Y. Chen, C. H. Hsu, C. Y. Ho, Computational fluid dynamics with application of different theoretical flow models for the evaluation of coronary artery stenosis on ct angiography: Comparison with invasive fractional flow reserve, *Biomed. Phys. Eng. Express*, **2** (2016), 065011. https://doi.org/10.1088/2057-1976/2/6/065011
9. A. Dubey, B. Vasu, O. Anwar Beg, R. S. R. Gorla, A. Kadir, Computational fluid dynamic simulation of two-fluid non-newtonian nanohemodynamics through a diseased artery with a stenosis and aneurysm, *Comput. Methods Biomech. Biomed. Eng.*, **23** (2020), 345–371. https://doi.org/10.1080/10255842.2020.1729755
10. E. C. Mason, S. McGhee, K. Zhao, T. Chiang, L. Matrka, The application of computational fluid dynamics in the evaluation of Laryngotracheal Pathology, *Ann. Otol. Rhinol. Laryngol.*, **128** (2019), 453–459. https://doi.org/10.1177/0003489419826601
11. C. Zhang, B. Lin, D. Li, Y. Fan, Application of multiscale coupling models in the numerical study of circulation system, *Med. Novel Technol. Devices*, **14** (2022), 100117. https://doi.org/10.1016/j.medntd.2022.100117
12. L. Liang, M. Liu, C. Martin, W. Sun, A deep learning approach to estimate stress distribution: a fast and accurate surrogate of finite-element analysis, *J. R. Soc. Intrface*, **15** (2018), 20170844. https://doi.org/10.1098/rsif.2017.0844
13. G. Hajgato, B. Gyires-Toth, G. Paal, Accelerating convergence of fluid dynamics simulations with convolutional neural networks, *Period. Polytech. Mech. Eng.*, **63** (2019), 230–239. https://doi.org/10.1098/rsif.2017.0844
14. G. Y. Li, H. R. Wang, M. Z. Zhang, S. Tupin, A. K. Qiao, Y. J. Liu, et al., Prediction of 3D cardiovascular hemodynamics before and after coronary artery bypass surgery via deep learning, *Commun. Biol.*, **4** (2021), 1–12. https://doi.org/10.1038/s42003-020-01638-1
15. L. Liang, W. Mao, W. Sun, A feasibility study of deep learning for predicting hemodynamics of human thoracic aorta, *J. Biomech.*, **99** (2020), 109544. https://doi.org/10.1016/j.jbiomech.2019.109544

16. G. Kissas, Y. B. Yang, E. Hwuang, W. R. Witschey, J. A. Detre, P. Perdikaris, Machine learning in cardiovascular flows modeling: predicting arterial blood pressure from non-invasive 4D flow MRI data using physics-informed neural networks, *Comput. Methods Appl. Eng.*, **358** (2020), 112623. https://doi.org/10.1016/j.cma.2019.112623
17. G. E. Karniadakis, I. G. Kevrekidis, L. Lu, P. Perdikaris, S. F. Wang, L. Yang, Physics-informed machine learning, *Nat. Rev. Phys.*, **3** (2021), 422–440. https://doi.org/10.1038/s42254-021-00314-5
18. M. Raissi, A. Yazdani, G. E. Karniadakis, Hidden fluid mechanics: learning velocity and pressure fields from flow visualizations, *Science*, **367** (2020), 1026–1030. https://doi.org/10.1126/science.aaw4741
19. S. Z. Cai, Z. P. Mao, Z. C. Wang, M. L. Yin, G. E. Karniadakis, Physics-informed neural networks (pinns) for fluid mechanics: a review, *Acta Mech. Sinica*, **37** (2021), 1729–1740. https://doi.org/10.1007/s10409-021-01148-1
20. M. Alber, A. B. Tepole, W. R. Cannon, S. De, S. Dura-Bernal, K. Garikipati, et al., Integrating machine learning and multiscale modeling-perspectives, challenges, and opportunities in the biological, biomedical, and behavioral sciences, *NPJ Digital Med.*, **2** (2019), 115. https://doi.org/10.1038/s41746-019-0193-y
21. E. Weinan, Machine learning and computational mathematics, *Commun. Comput. Phys.*, **28** (2020), 1639–1670. https://doi.org/10.4208/cicp.OA-2020-0185
22. L. Huan, W. Lei, E. Weinan, Machine-learning-based non-newtonian fluid model with molecular fidelity, *Phys. Rev. E*, **102** (2020), 043309. https://doi.org/10.1103/PhysRevE.102.043309
23. E. Samaniego, C. Anitescu, S. Goswami, V. M. Nguyen-Thanh, H. Guo, K. Hamdia, et al., An engergy approach to the solution of partial differential equations in computational mechanics via machine learning: concepts, implementation, and applications, *Comput. Methods Appl. Mech. Eng.*, **362** (2020), 112790. https://doi.org/10.1016/j.cma.2019.112790
24. N. Sukumar, A. Srivastava, Exact imposition of boundary conditions with distance functions in physics-informed deep neural networks, *Comput. Methods Appl. Mech. Eng.*, **389** (2022), 114333. https://doi.org/10.1016/j.cma.2021.114333
25. X. W. Jin, S. Z. Cai, H. Li, G. E. Karniadakis, NSFnets (Navier-Stokes Flow Nets): physics-informed neural networks for the incompressible Navier-Stokes equations, *J. Comput. Phys.*, **426** (2021), 109951. https://doi.org/10.1016/j.jcp.2020.109951
26. A. Valencia, F. Solis, Blood flow dynamics and arterial wall interaction in a saccular aneurysm model of the basilar artery, *Comput. Struct.*, **84** (2006), 1326–1337. https://doi.org/10.1016/j.compstruc.2006.03.008
27. M. Tremmel, S. Dhar, E. I. Levy, J. Mocco, H. Meng, Influence of Intracranial aneurysm-to-parent vessel size ratio on hemodynamics and implication for rupture: results from a virtual experimental study, *Neurosurgery*, **64** (2009), 622–630. https://doi.org/10.1227/01.NEU.0000341529.11231.69
28. K. M. Tse, R. Chang, H. P. Lee, S. P. Lim, S. K. Venkatesh, P. Ho, A computational fluid dynamics study on geometrical influence of the aorta on hemodynamics, *Eur. J. Cardio-Thoracic Surg.*, **43** (2012), 829–838. https://doi.org/10.1093/ejcts/ezs388
29. M. Simao, J. Ferreira, A. C. Tomas, J. Fragata, H. Ramos, Aorta ascending aneurysm analysis using CFD models towards possible anomalies, *Fluid*, **2** (2017), 31. https://doi.org/10.3390/fluids2020031

30. R. Savabi, M. Nabaei, S. Farajollahi, N. Fatouraee, Fluid structure interaction modeling of aortic arch and carotid bifurcation as the location of baroreceptors, *Int. J. Mech. Sci.*, **165** (2020), 105222. https://doi.org/10.1016/j.ijmecsci.2019.105222
31. M. Raissi, Z. C. Wang, M. S. Triantafyllou, G. E. Karniadakis, Deep learning of vortex induced vibrations, *J. Fluid Mech.*, **861** (2019), 119–137. https://doi.org/10.1017/jfm.2018.872
32. J. Lin, S. Zhou, H. Guo, A deep collocation method for heat transfer in porous media: verification from the finite element method, *J. Energy Storage*, **28** (2020), 101280. https://doi.org/10.1016/j.est.2020.101280
33. K. M. Hamdia, X. Zhuang, T. Rabczuk, An efficient optimization approach for designing machine learning models based on genetic algorithm, *Neural Comput. Appl.*, **33** (2021), 1923–1933. https://doi.org/10.1007/s00521-020-05035-x
34. A. Kendall, Y. Gal, R. Cipolla, Multi-task learning using uncertainty to weigh losses for scene geometry and semantics, in *Proceedings of the IEEE Computer Society*, *Conference on Computer Vision and Pattern Recognition*, IEEE Computer Society, (2018), 7482–7491. https://doi.org/10.1109/CVPR.2018.00781
35. K. H. Thung, C. Y. Wee, A brief review on multi-task learning, *Multimedia Tools Appl.*, **77** (2018), 29705–29725. https://doi.org/10.1007/s11042-018-6463-x
36. M. L. Wang, H. X. Li, X. Chen, Y. Chen, Deep learning-based model reduction for distributed parameter systems, *IEEE Trans. Syst. Man Cybern.-Syst.*, **46** (2016), 1664–1674. https://doi.org/10.1109/TSMC.2016.2605159